# POD study on the mechanism of turbulent drag reduction and heat transfer reduction based on Direct Numerical Simulation

Yi Wang, Bo Yu* and Xuan Wu

Beijing Key Laboratory of Urban Oil
and Gas Distribution Technology,
China University of Petroleum-Beijing,
Beijing 102249, China
E-mail: wy1031@yahoo.com.cn
E-mail: yubobox@cup.edu.cn
E-mail: wuxuancup@yahoo.cn
*Corresponding author

Jinjia Wei

State Key Laboratory of Multiphase Flow
in Power Engineering,
Xi'an Jiaotong University,
Xi'an 710049, China
E-mail: jjwei@mail.xjtu.edu.cn

Fengchen Li

School of Energy Science and Engineering,
Harbin Institute of Technology,
Harbin 150001, China
E-mail: lifch@hit.edu.cn

Yasuo Kawaguchi

Department of Mechanical Engineering,
Tokyo University of Science,
Yamazaki 2641, Noda, Chiba 278-8510, Japan
E-mail: yasuo@rs.noda.tus.ac.jp

**Abstract:** Direct Numerical Simulations (DNSs) have been performed for turbulent channel flows of Newtonian fluid and drag-reducing fluid with heat transfer. Main coherent structures in the drag-reducing flow and heat transfer were extracted from the DNS database by Proper Orthogonal Decomposition (POD) method. The mechanisms of turbulent drag reduction and heat transfer reduction were studied through the analyses of the coherent structures and energy distribution reflected by different POD eigenmodes.

**Keywords:** POD; DNS; drag reduction; heat transfer reduction; computational fluid dynamics.

**Reference** to this paper should be made as follows: Wang, Y., Yu, B., Wu, X., Wei, J.J., Li, F.C. and Kawaguchi, Y. (2011) 'POD study on the mechanism of turbulent drag reduction and heat transfer reduction based on Direct Numerical Simulation', *Progress in Computational Fluid Dynamics*, Vol. 11, Nos. 3/4, pp.149–159.

This paper is a revised and expanded version of a paper entitled 'DNS Study on Heat Transfer Reduction of Drag-Reducing Channel Flow Induced by Surfactant Additives With a Bilayer Model' presented at *Asian Symposium on Computational Heat Transfer and Fluid Flow*, Jeju, Korea, 20–23 October, 2009.

## 1 Introduction

The POD was first proposed by Lumley (1967). It has become a technology to obtain large-scale structures or coherent structures, which are very important in turbulent flows. These structures are mathematically independent and contain different magnitudes of energy, corresponding to different POD eigenmodes. Early applications of the POD method were made by Bakewell and Lumley (1967) for a turbulent pipe flow and by Payne and Lumley (1967) for turbulent flow across a cylinder. However, they only obtained the first eigenmodes because their experimental data were not dense enough. Sirovich (1987) proposed the snapshot form of POD, which largely reduced the processing time and difficulty. Deane et al. (1991) studied transition flows in grooved channels and circular cylinders by the POD method. They found that the systems can be predicted very well using only 4–8 eigenmodes. Rajaee et al. (1994) analysed the coherent structures in free shear layer flows and found that the first certain POD eigenmodes contained most fluctuating energy. Rempfer and Fasel (1994a, 1994b) studied the coherent structures in a flat plate boundary layer. The results showed that the dynamics of the coherent structures can be described accurately by POD eigenmodes. The first eigenmode was in good agreement with the large-scale structures by experiments. Other researchers combined Particle Image Velocimetry (PIV) technique with 'snapshot' POD to extract large-scale coherence of fluctuations from experimental data (Bernero and Fiedler, 2000; Laurent et al., 2001; Gurka et al., 2006; Druault and Chaillou, 2007; Shi et al., 2010).

With the development of Computational Fluid Dynamics (CFD), DNS has been a powerful tool for mechanism study of turbulent flow and heat transfer. It can provide detailed information in whole flow field so that snapshots are much more than experimental approaches. Therefore, POD analysis or modelling based on DNS data has been a new approach to study the coherent structures and energy distribution in turbulence more precisely. Moin and Moser (1989) applied POD to DNS study on turbulent channel flow and obtained a main structure containing over 70% turbulent kinetic energy. Ball et al. (1991) processed the data of turbulent channel flow by POD and found more than 75% turbulent kinetic energy distributed in about 25 POD eigenmodes. Gatski and Glauser (1992) established a POD model to reconstruct the turbulent kinetic energy, shear stress and dissipation and so on. Yang et al. (2010) dealt with the DNS database in an orthogonally rotating turbulent duct flow to study the influence of buoyancy on turbulent large-scale structures and the energy distributions in POD eigenmodes. They pointed out that the turbulent large-scale structures mainly locate in the unstable wall and near the sidewalls; with the increase of the Grashof number, the most of the turbulent kinetic energy distributes into more POD eigenmodes.

However, most POD analyses have been focused on the Newtonian fluid flow, based on either experiments or numerical computations. The POD analysis for drag-reducing flow seems first made by Cai et al. (2009) combining with PIV measurements. Some researchers were trying to discover the mechanisms of drag reduction and heat transfer reduction by DNS (Yu and Kawaguchi, 2005; Kagawa et al., 2008; Wang et al., 2009; Yu et al., 2011). Although the drag reduction by a small amount of surfactant additives into turbulent flow is very meaningful for saving a large amount of energy, its application is limited by heat transfer reduction accompanying drag reduction. Yu et al. (2011) employed a bilayer model with coexisting Newtonian fluid and drag-reducing fluid to do the DNS study. They discovered the most effective region of surfactant network structure and the wall-normal turbulent heat flux decreased as drag-reducing flow layer expanded. In the present study, POD method is introduced to analyse the DNS data of both Newtonian fluid flow and drag-reducing flow. It is expected to clarify proper information about mechanisms of drag reduction and heat transfer reduction by extracting multi-scale structures and energy distribution from DNS.

## 2 Physical model and governing equation

DNSs of fully developed turbulent channel flows of viscoelastic drag-reducing fluid and Newtonian fluid have been carried out. Figure 1 illustrates the flow geometry and the coordinates. The $x$, $y$ and $z$ represent the streamwise, wall-normal and spanwise directions, respectively, and the corresponding velocity components are $u$, $v$ and $w$. The viscoelastic fluid is assumed to be incompressible and isothermal and having constant properties. Periodic boundary conditions are imposed in both the streamwise ($x$–) and spanwise ($z$–) directions, while the non-slip boundary condition is adopted for the top and bottom walls. A computational domain $10h \times 2h \times 5h$ in the streamwise, wall-normal and spanwise directions, respectively, is chosen. For the simulation of the three-dimensional time-dependent incompressible viscoelastic flow, dimensionless differential equations (one for the continuity equation, three for the velocity components and six for extra stress components) are to be solved as follows:

Continuity equation:

$$\frac{\partial u_i^+}{\partial x_i^*} = 0 \tag{1}$$

Momentum equation:

$$\frac{\partial u_i^+}{\partial t^*} + u_j^+ \frac{\partial u_i^+}{\partial x_j^*} = -\frac{\partial p^{+*}}{\partial x_i^*} + \frac{1}{Re_\tau}\frac{\partial}{\partial x_j^*}\left(\frac{\partial u_i^+}{\partial x_j^*}\right) + \frac{\beta}{We_\tau}\frac{\partial c_{ij}^+}{\partial x_j^*} + \delta_{1i} \tag{2}$$

Giesekus constitutive equation:

$$\frac{\partial c_{ij}^{+}}{\partial t^{*}}+\frac{\partial u_{m}^{+}c_{ij}^{+}}{\partial x_{m}^{*}}-\frac{\partial u_{i}^{+}}{\partial x_{m}^{*}}c_{mj}^{+}-\frac{\partial u_{j}^{+}}{\partial x_{m}^{*}}c_{mi}^{+}+\frac{Re_{\tau}}{We_{\tau}}\left[-\delta_{ij}+c_{ij}^{+}+\alpha(c_{im}^{+}-\delta_{im})(c_{mj}^{+}-\delta_{mj})\right]=0 \tag{3}$$

Energy equation:

$$\frac{\partial \theta^{+}}{\partial t^{*}}+u_{j}^{+}\frac{\partial \theta^{+}}{\partial x_{j}^{*}}=\frac{2u^{+}}{\int_{-1}^{1}U^{+}\mathrm{d}y^{*}}+\frac{1}{Re_{\tau}Pr}\frac{\partial}{\partial x_{j}^{*}}\left(\frac{\partial \theta^{+}}{\partial x_{j}^{*}}\right) \tag{4}$$

The momentum equation of Newtonian fluid flow is Navier-Stokes equation while the continuity equation and the energy equation are the same as Equations (1) and (4). Hence, they are neglected here. For drag-reducing fluid flow, $We_{\tau}=25$, $\alpha=0.001$ and $\beta=0.1$; for both Newtonian fluid and drag-reducing fluid flows, $Re_{\tau}=125$ and $Pr=0.71$.

**Figure 1** Computational domain of channel flow

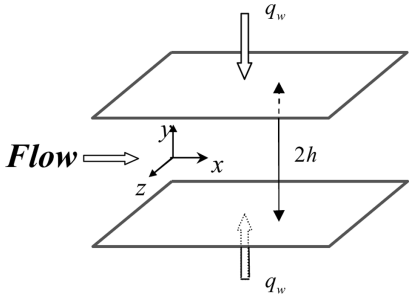


DNS is made by discretision of the governing equations above. The computations are carried out with a mesh of $64\times64\times64$ grid points, which has been proved dense enough to sustain the turbulence (Yu et al., 2011). Uniform grids are used in the streamwise and spanwise directions. Non-uniform grids are used in the wall-normal direction with denser mesh near the wall to resolve small eddies. The computational algorithm is a fractional step method using the Adams-Bashforth scheme for the time advancement with the dimensionless time step $2\times10^{-4}$. The convective and diffusion terms in the momentum equations are discretised by a fourth order central compact difference scheme to achieve high accuracy. The convective terms in the Giesekus constitutive equations are discretised by MINMOD scheme to enhance the numerical stability (Yu and Kawaguchi, 2004). To avoid a zigzag pressure field, staggered grids are used in which pressure and conformation components are stored at the cell centre while velocity components are located at the cell borders.

## 3 POD method

200 snapshots of the velocity and temperature field are obtained by DNS for POD analysis. Firstly, the mean fields can be obtained:

$$\overline{F(\vec{X})}=\frac{1}{N}\sum_{i=1}^{N}F(\vec{X},t_{i}^{*}) \tag{5}$$

where $F$ is a common variable for $u^{+}$, $v^{+}$, $w^{+}$, $\theta^{+}$, $\vec{X}$ represents $x^{*}$, $y^{*}$, $z^{*}$, $N$ is the number of snapshots, '—' stands for mean values.

Fluctuating field can be extracted from the instantaneous field and the mean field:

$$F'(\vec{X},t_{i}^{*})=F(\vec{X},t_{i}^{*})-\overline{F(\vec{X})}\quad(i=1,2,\ldots,N). \tag{6}$$

The snapshot POD method is applied to the fluctuating field in the following steps:

1 Get the inner product in the Hilbert space:

$$C_{ij}=\frac{1}{N}\int_{\Omega}F'(\vec{X},t_{i}^{*})F'(\vec{X},t_{j}^{*})d\Omega\quad(i=1,2,\ldots,N,\ j=1,2,\ldots,N). \tag{7}$$

2 Get the eigenvalues and eigenvectors by singular value decomposition of the inner product $C$:

$$CA=\lambda A \tag{8}$$

where $\lambda$ is eigenvalue, $A$ is eigenvector corresponding to $\lambda$.

3 Get POD eigenmodes from the eigenvectors and the fluctuating field:

$$\phi_{k}(\vec{X})=\sum_{i=1}^{N}A_{ki}F'(\vec{X},t_{i}^{*}) \tag{9}$$

where $k$ represents the $k$th POD eigenmode.

4 Get temporal coefficients from the POD eigenmodes and the fluctuating field:

$$\alpha_{k}(t_{i}^{*})=\int_{\Omega}F'(\vec{X},t_{i}^{*})\phi_{k}(\vec{X})\mathrm{d}\Omega\quad(i=1,2,\ldots,N). \tag{10}$$

5 Reconstruct a new fluctuating field from the coefficients and POD eigenmodes:

$$f'(\vec{X},t_{i}^{*})=\sum_{k=1}^{N_{1}}\alpha_{k}(t_{i}^{*})\phi_{k}(\vec{X})\quad(N_{1}\le N,i=1,2,\ldots,N). \tag{11}$$

The main purpose of this study is to extract main structures of velocity field and temperature field, not establishing a POD model. Thus, only steps 1–3 have been done for studying energy distribution and coherent structures. The coherent structures can be obtained by analysing the POD eigenmodes of the fluctuating field. The total energy of the fluctuating field can be calculated by the sum of the eigenvalues:

$$E=\sum_{n=1}^{N}\lambda_{n}. \tag{12}$$

Thus, the magnitude of the $n$th eigenvalue $\lambda_{n}$ represents the energy relative contribution to the total energy in the $n$th eigenmode $\phi_{n}$:

$$\xi_n = \frac{\lambda_n}{\sum_{n=1}^{N} \lambda_n}. \tag{13}$$

The cumulative energy relative contribution to the total energy, i.e., the summation of the energy relative contributions for the first $N_1$ eigenmodes is:

$$\zeta_n = \frac{\sum_{n=1}^{N_1} \lambda_n}{\sum_{n=1}^{N} \lambda_n}. \tag{14}$$

## 4 Results and discussion

Drag-reduction rate is defined as the reduction of friction factor for Newtonian fluid flow at equal mean Reynolds number $Re_m$.

$$DR\% = \frac{C_f^D - C_f}{C_f^D} \times 100\%. \tag{15}$$

$C_f^D$ is evaluated by Dean's equation $C_f^D = 0.073 Re_m^{-0.25}$ (Dean, 1978). The heat transfer reduction rate $HTR$% is defined as the reduction of Nusselt number for the Newtonian fluid flow at the same mean Reynolds number $Re_m$,

$$HTR\% = \frac{Nu^K - Nu}{Nu^K} \times 100\%. \tag{16}$$

$Nu^K$ is calculated by Kays and Crawford's equation $Nu^K = 0.022 Re_m^{0.8} Pr^{0.5}$ (Kays and Crawford, 1980). The drag-reduction rate and heat transfer reduction rate obtained in this DNS study are 31% and 35%, respectively.

Figure 2 is the mean velocity profile and mean temperature profile. In the viscous sublayer, mean velocity and mean temperature are in good agreement with linear distribution respectively: $U^+ = y^+$ and $\Theta^+ = Pr \cdot y^+$. In the buffer layer, mean velocity and mean temperature of drag-reducing flow increase significantly compared to those of Newtonian fluid flow. All the analyses above confirm that the buffer layer is the most effective region for drag-reducing additives to induce drag reduction and heat transfer reduction and demonstrate that velocity profile and temperature profile have many similarities.

Figure 3 shows the velocity fluctuation intensities in the three directions and temperature fluctuation intensity. The streamwise velocity fluctuation intensity of drag-reducing flow becomes larger than Newtonian fluid flow and its peak value position shifts to the bulk flow region. The other two components of velocity fluctuation intensities are depressed by drag-reducing additives. For drag-reducing flow, the peak value position of temperature fluctuation ($y^+ = 25$) is much closer to the bulk flow region than that of streamwise velocity fluctuation ($y^+ = 22$). This may be an important reason that heat transfer reduction is greater than drag reduction.

The energy relative contributions to the total energy of each POD eigenmode obtained from the fluctuating field are compared in Figure 4. The first eigenmode, which has the highest energy contribution, contains the main energy of flow indicating that it may capture the largest scale vortex structure. The contributions of the following eigenmodes decrease, representing that the structure scales of flow and heat transfer become smaller. For drag-reducing flow, the energy contributions of the first amount of POD eigenmodes are higher than those of Newtonian fluid flow. The increment decreases from the first eigenmode to the last one. The contributions of the latter eigenmodes are lower than Newtonian fluid flow. These phenomena show that drag-reducing additives mainly affect large-scale structures containing main turbulent kinetic energy.

**Figure 2** Mean profiles of velocity and temperature: (a) Mean velocity profile and (b) mean temperature profile

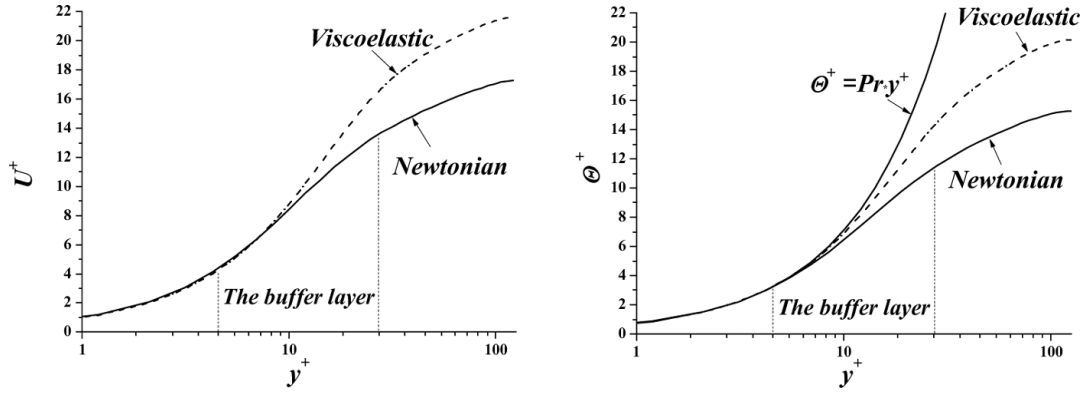


(a) (b)

The cumulative energy contributions of the POD eigenmodes are shown in Figure 5. For Newtonian fluid flow, the curve is flat, showing that all scale structures play important roles to the total energy and no dominant structure exists that contains the most energy. The convergence of the cumulative energy contribution of drag-reducing flow is much faster than that of Newtonian fluid flow. It is contacted with the

increasing proportion of large-scale structures and decreasing proportion of small-scale structures in the energy spectrum.

It can also be seen from Figures 4 and 5 that the energy distribution changes of $u'^{+}$ and $\theta'^{+}$ are much greater than those of $v'^{+}$ and $w'^{+}$. Taking the first POD eigenmode as an example, the energy contribution for $u'^{+}$ increases from about 2.5% for Newtonian fluid flow to about 12.5% for drag-reducing flow. The energy contribution for $\theta'^{+}$ increases from about 5.5% to about 11%. However, the energy contribution of the first POD eigenmode only increases within the value of 1% for $v'^{+}$ and $w'^{+}$. Therefore, $u'^{+}$ and $\theta'^{+}$ are main fluctuations, and the flow and heat transfer become further anisotropic for drag-reducing flow. The POD eigenmodes of these main fluctuations will be analysed to extract the proper characteristics of flow and heat transfer. Two typical POD eigenmodes are selected, i.e., the eigenmodes with the highest energy contribution and the lowest energy contribution.

Figure 6 compares the typical POD eigenmodes of $u'^{+}$ in the *x*-*y* plane located at the middle *z*. 'a' and 'b' represent the first and the last POD eigenmode, respectively. '1' and '2' represent Newtonian fluid flow and drag-reducing flow, respectively. It can be seen that the POD eigenmodes with the highest and lowest energy contribution contain large-scale and small-scale fluctuation structures, verifying the analyses in Figures 4 and 5. The large-scale structure of drag-reducing flow enlarges apparently compared to that of Newtonian fluid flow but the small-scale structures have no big differences. These indicate that energy contribution is corresponding to the scale of the fluctuating structure. The larger scale structure contains relatively higher energy, representing the main characteristic of flow. It is clear from Figure 6(a1) and (a2) that the fluctuating structures of drag-reducing flow are enlarged and the fluctuation gradient decreases in the wall-normal direction, reflecting the laminarisation of the fluctuating velocity field.

Figure 7 compares the typical POD eigenmodes of $u'^{+}$ in the *x*-*z* plane located at $y^{+}=5$. For both Newtonian fluid flow and drag-reducing flow, the POD eigenmodes with higher energy represent larger scale fluctuating structures (column a), showing proper characteristics of high-speed and low-speed streaks. It reflects the alternation of streamwise fluctuation in different directions and at different intensities, i.e., the strong positive fluctuations and the strong negative fluctuations appear in turn. The transitional area between these two strong fluctuation areas contains weak fluctuations, which are the superposition of the two strong fluctuations in the opposite directions. The POD eigenmodes with lower energy capture small and random structures (column b), showing the small-scale fluctuations caused by the collision and mix of different speed fluids.

**Figure 3** Velocity fluctuation intensities and temperature fluctuation intensity: (a) streamwise velocity fluctuation intensity; (b) wall-normal velocity fluctuation intensity; (c) spanwise velocity fluctuation intensity and (d) temperature fluctuation intensity

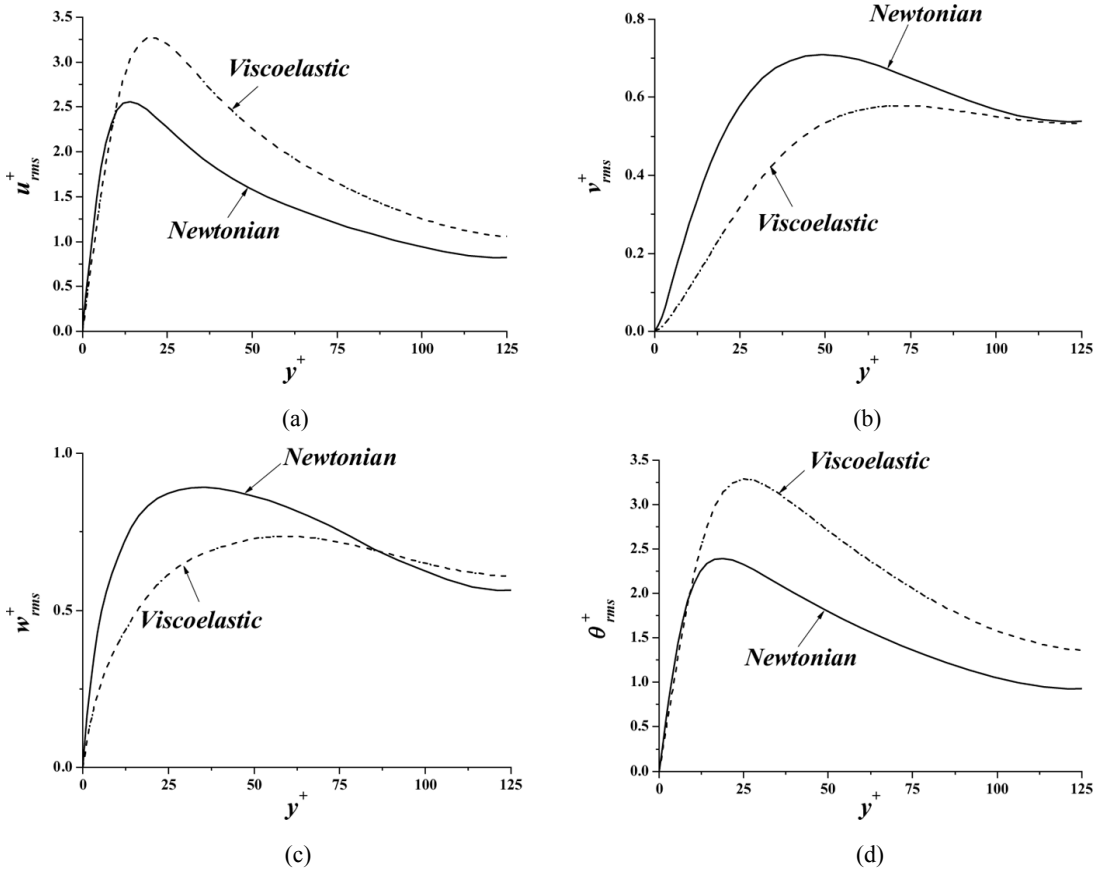

**Figure 4** Energy contributions for different POD eigenmodes: (a) $u'^{+}$; (b) $v'^{+}$; (c) $w'^{+}$ and (d) $\theta'^{+}$

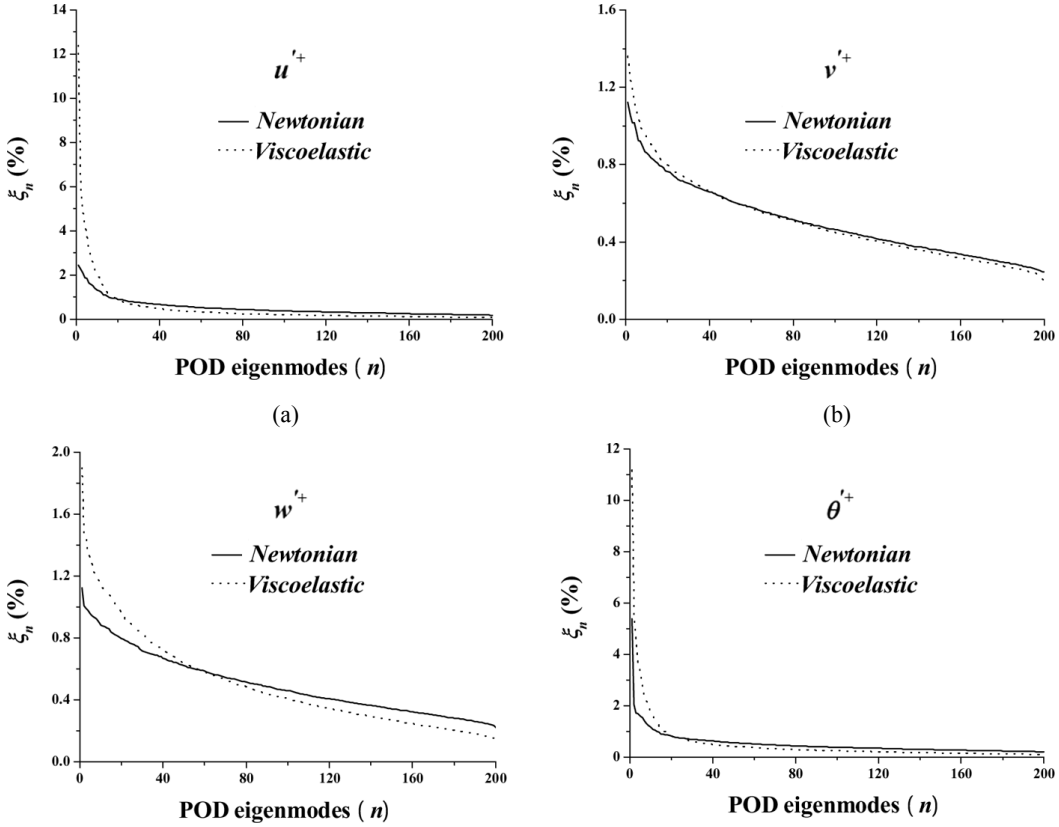


**Figure 5** Cumulative energy contributions for different POD eigenmodes: (a) $u'^{+}$; (b) $v'^{+}$; (c) $w'^{+}$ and (d) $\theta'^{+}$

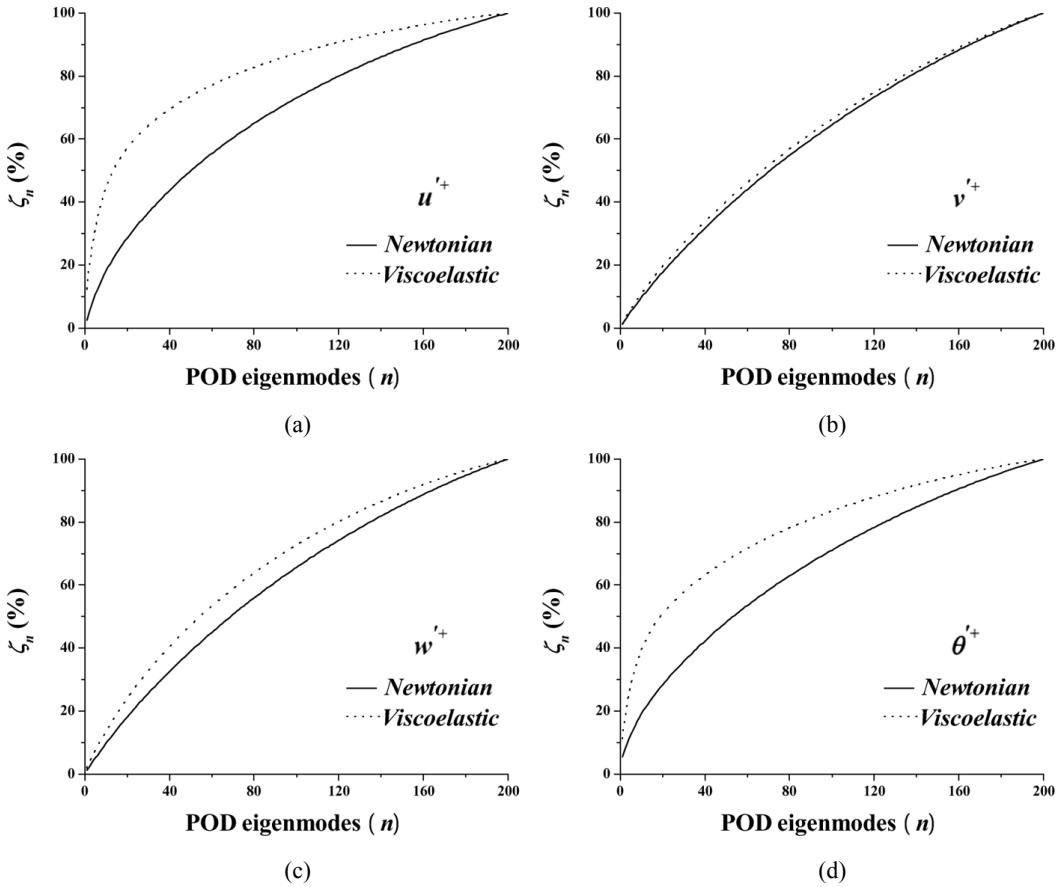

**Figure 6** Typical POD eigenmodes of $u'^{+}$ in the *x*-*y* plane located at the middle *z*: 'a' – the first POD eigenmode; 'b' – the last POD eigenmode; '1' – Newtonian fluid flow; '2' – drag reducing flow

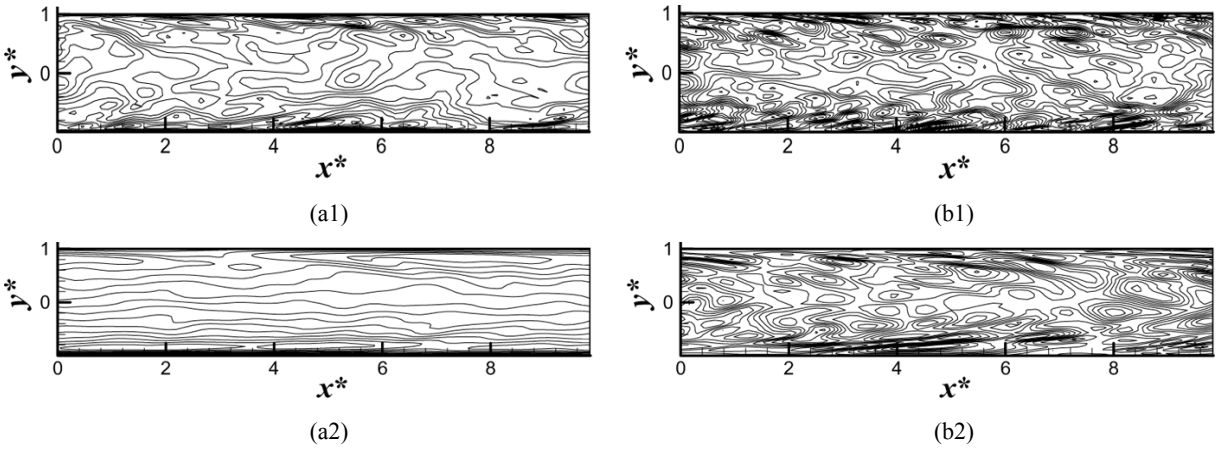


**Figure 7** Typical POD eigenmodes of $u'^{+}$ in the *x*-*z* plane near wall: 'a' – the first POD eigenmode; 'b' – the last POD eigenmode; '1' – Newtonian fluid flow; '2' – drag reducing flow

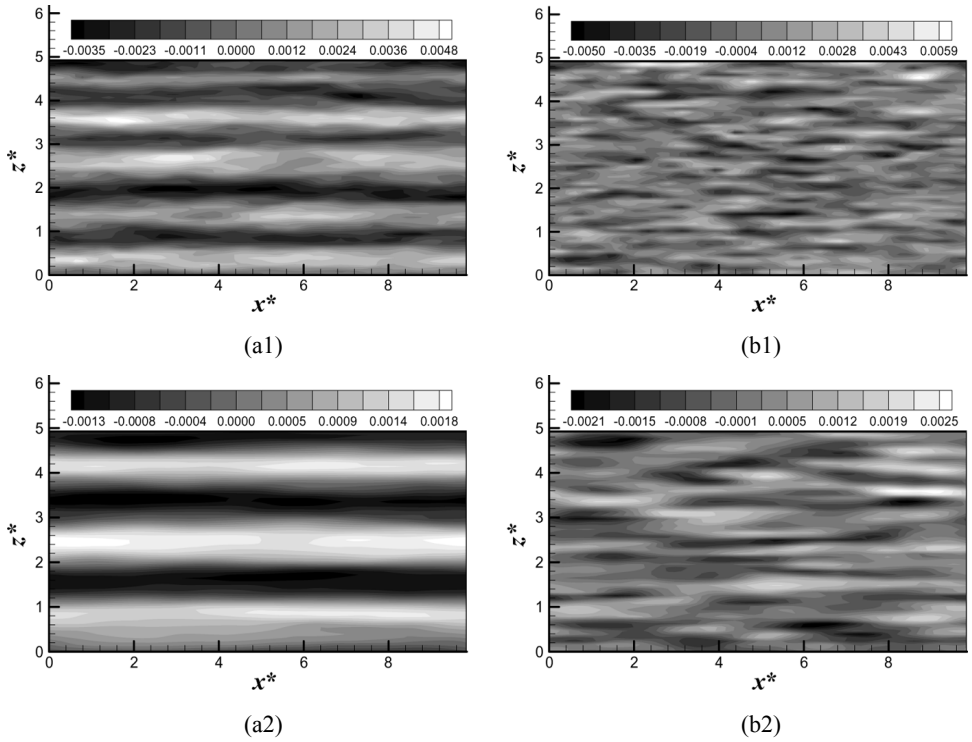


For drag-reducing flow, the values of POD eigenmodes (Fig. 7(a2)) are much smaller than those of Newtonian fluid flow (Fig. 7(a1)). Correspondingly, the large-scale structures are clearer and the widths of these structures become larger. Meanwhile, the small-scale structures become slimmer. These phenomena demonstrate that the fluctuation intensity of drag-reducing flow is depressed near the wall and the constitution of kinetic energy is changed. The small-scale fluctuating structures are suppressed, reducing the proportion of turbulent kinetic energy dissipation to the total kinetic energy. The large-scale structures are enhanced, storing higher proportion of turbulent kinetic energy. In all, the coherent structures near the wall are further organised and flow field develops to the aspect with lower dissipation of turbulent kinetic energy.

Figure 8 is the typical POD eigenmodes of $u'^{+}$ in the *y*-*z* plane located at the middle *x*. The POD eigenmodes with higher energy mainly capture larger scale fluctuating structures near walls (column a), whereas the POD eigenmodes with lower energy mainly capture small-scale random fluctuating structures (column b). The large-scale structures of drag-reducing flow (Fig. 8(a2)) are larger than those of Newtonian fluid flow (Fig. 8(a1)), arranging in order along the spanwise direction. In this case, the whole *y*-*z* plane is occupied by these large-scale structures (Fig. 8(a2)), without any medium- and small-scale structures in Newtonian fluid flow (Fig. 8(a1)). Moreover, it is also found in Figure 8(a2) that the large-scale structures exist in pairs, i.e., one positive large-scale structure always appears with one negative large-scale structure. All the

phenomena above indicate that drag-reduction is related to the alternative existence of a series of clockwise and counterclockwise vortex structures. From Figure 8(b1) and (b2), it can be seen that the near wall ($-1 < y^* < -0.9$ and $0.9 < y^* < 1$) small-scale structures in drag-reducing flow become larger and their number becomes smaller than those in Newtonian fluid flow, showing the energy contributions of the small-scale structures decrease compared to those of Newtonian fluid flow.

The typical POD eigenmodes of $\theta'^{+}$ are compared in the three typical planes shown in Figures 9–11. In the *x*-*y* plane (Fig. 9), large-scale temperature structures mainly have *y*-gradient, showing main heat flux transfers to inner fluid by the wall-normal temperature gradient. For drag-reducing flow (Fig. 9(a2)), the large-scale structures containing main energy tend to be regular compared to those of Newtonian fluid flow. It reflects the depression of heat convection and the characteristics of heat transfer are closer to heat conduction, which may be an important reason of the heat transfer reduction. The chaotic small structures in Figure 9(b1) and (b2) exhibit the small-scale temperature fluctuations and irregular molecular motions have no big changes in the streamwise direction between drag-reducing flow and Newtonian fluid flow.

**Figure 8** Typical POD eigenmodes of $u'^{+}$ in the *y*-*z* plane located at the middle *x*: 'a' – the first POD eigenmode; 'b' – the last POD eigenmode; '1' – Newtonian fluid flow; '2' – drag reducing flow

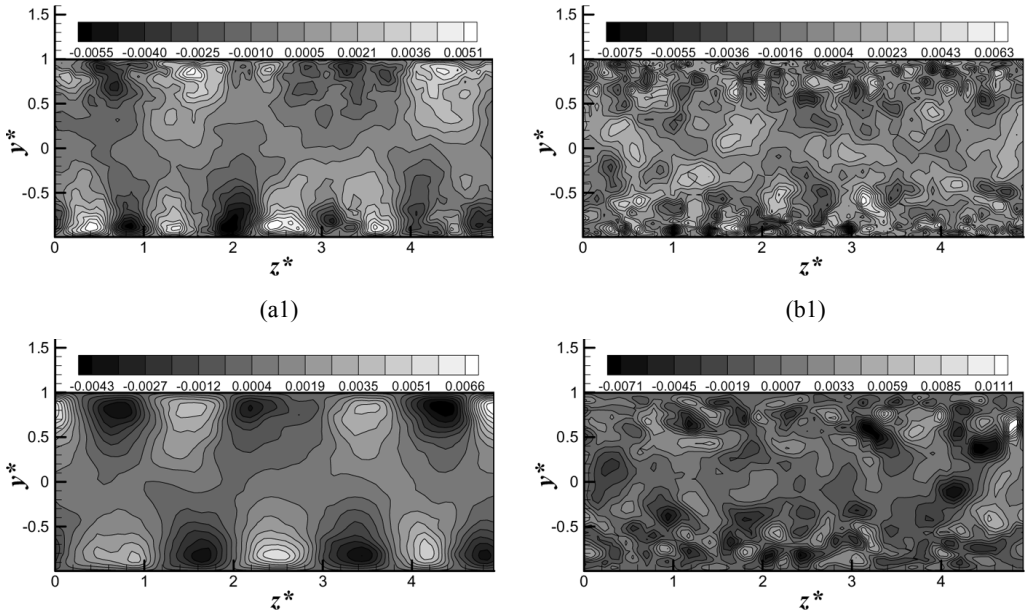


**Figure 9** Typical POD eigenmodes of $\theta'^{+}$ in the *x*-*y* plane located at the middle *z*: 'a' – the first POD eigenmode; 'b' – the last POD eigenmode; '1' – Newtonian fluid flow; '2' – drag reducing flow

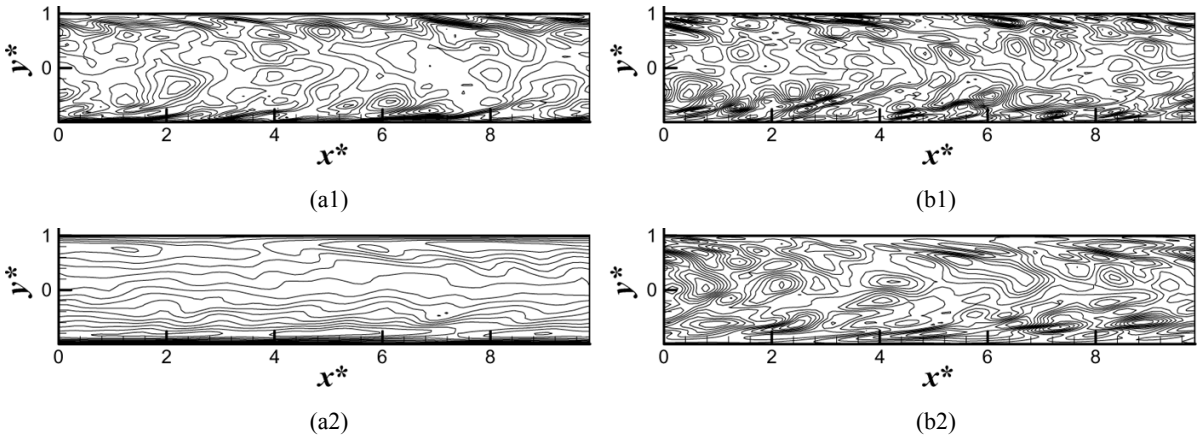


In the *x*-*z* plane (Fig. 10), the captured large- and small-scale structures of Newtonian fluid flow are tiny and short indicating the heat transfer between high- and low-temperature fluids is good (Fig. 10(a1) and (b1)). When the drag-reducing additives exist, the temperature streaks captured by the first POD eigenmode become larger and the distinction between the high- and low-temperature streaks is much clearer (Fig. 10(a2)). The small-scale temperature fluctuations represented by the last POD eigenmode are in better order (Fig. 10(b2)) than those of

Newtonian fluid flow (Fig. 10(b1)). The variation shows that the temperature fluctuations are suppressed in all scales and arranged regularly. The suppression of the temperature fluctuations near the wall causes heat transfer reduction.

In the *y-z* plane (Fig. 11), all scale temperature structures of Newtonian fluid flow occupy the whole plane reflecting the active temperature fluctuation and heat transfer in all scales (Fig. 11(a1) and (b1)). For drag-reducing flow, the small-scale temperature structures are still active compared to those of Newtonian fluid flow (Fig. 11(b2)), but the large-scale temperature structures centralise near the walls (Fig. 11(a2)) and appear as clockwise and counterclockwise streamwise fluctuating structures alternately along the spanwise direction, causing the heat transfer ability of fluid in central area reduced.

**Figure 10** Typical POD eigenmodes of $\theta'^{+}$ in the *x-z* plane near wall: 'a' – the first POD eigenmode; 'b' – the last POD eigenmode; '1' – Newtonian fluid flow; '2' – drag reducing flow

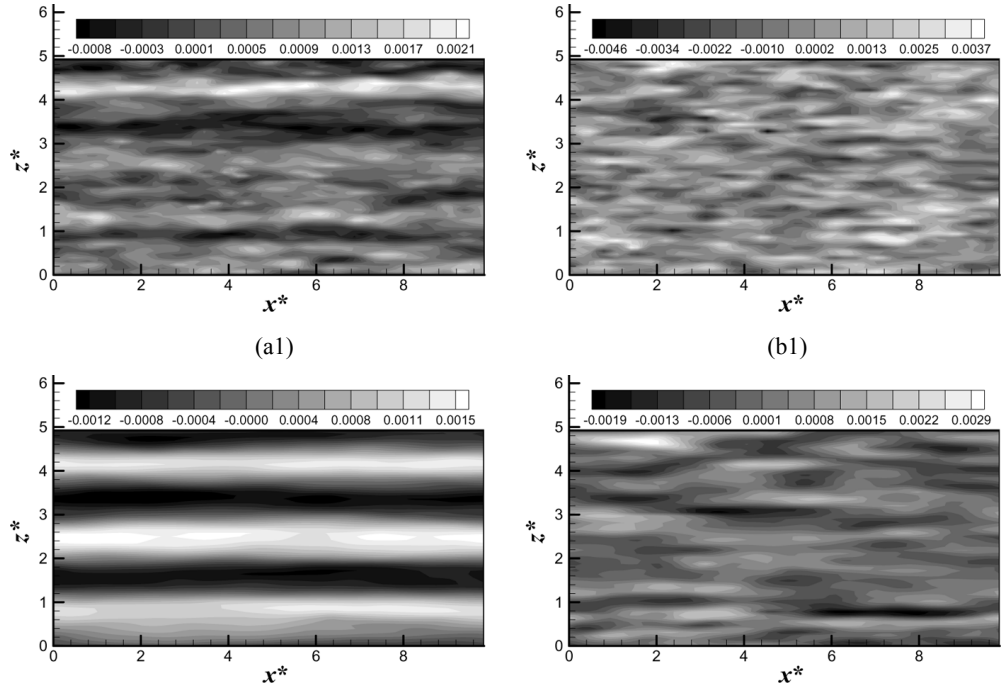


(a1) (b1)

(a2) (b2)

**Figure 11** Typical POD eigenmodes of $\theta'^{+}$ in the *y-z* plane located at the middle *x*: 'a' – the first POD eigenmode; 'b' – the last POD eigenmode; '1' – Newtonian fluid flow; '2' – drag reducing flow

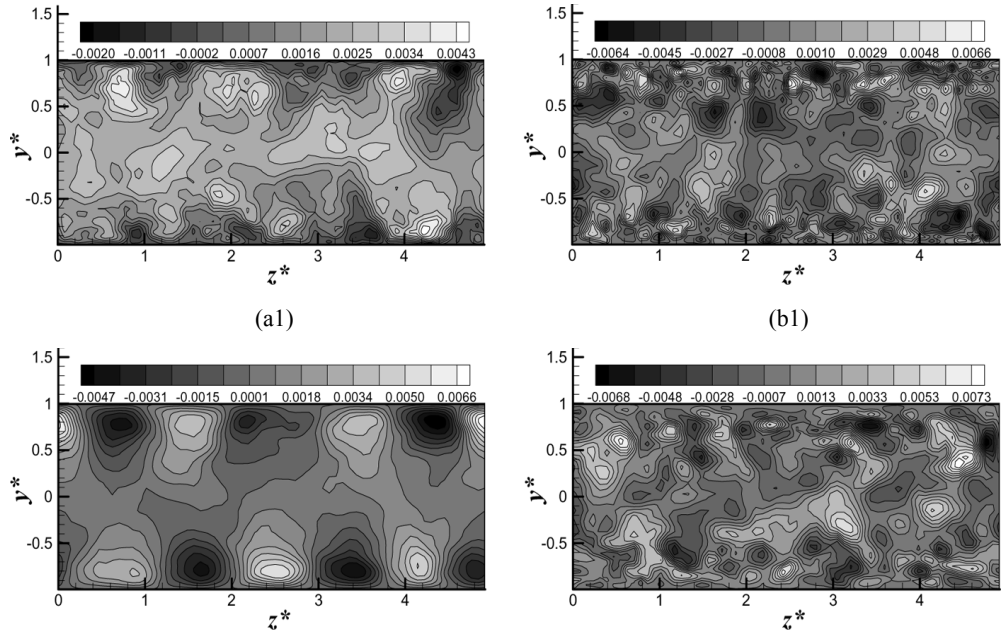


(a1) (b1)

(a2) (b2)

## 5 Conclusions

It can be seen from the analyses above that the large- and small-scale coherent structures extracted from the POD eigenmodes can represent main characteristics of drag reduction and heat transfer reduction. More detailed conclusions can be made as follows:

- Drag-reducing additives mainly affect large-scale structures, which contain main proportion of turbulent kinetic energy. The energy relative contribution to the total energy of the large-scale structures becomes larger, and the contribution of the small-scale structures, which represents energy dissipation, becomes smaller in drag-reducing fluid flow. These changes cause stronger anisotropy in flow and heat transfer characteristics of drag-reducing flow than those of Newtonian fluid flow.
- The energy distributions of streamwise velocity fluctuation and temperature fluctuation are affected by drag-reducing additives more deeply than those of velocity fluctuations in the wall-normal and the spanwise directions. For drag-reducing flow, the large-scale structures are enlarged in the streamwise direction and align in the spanwise direction alternately as well-organised clockwise and counterclockwise streamwise swirling motions. The gradient of these large-scale structures becomes smaller in the wall-normal direction. The large-scale temperature fluctuations concentrate near the walls of the channel while the main characteristic of heat transfer is closer to heat conduction. This may be an important reason of heat transfer reduction. The small-scale structures are weakened so the flow develops to the aspect of lower dissipation.

## Acknowledgements

The authors acknowledge the support from the National Natural Science Foundation of China (No. 50876114, No. 51076124, No.51076036), the State Key Laboratory of Multiphase Flow in Power Engineering (Xi'an Jiaotong University).

## References

Bakewell, H.P. and Lumley, J.L. (1967) 'Viscous sublayer and adjacent wall region in turbulent pipe flow', *Physics of Fluids*, Vol. 10, pp.1880–1889.

Ball, K.S., Sirovich, L. and Keefe, L.R. (1991) 'Dynamical eigenfunction decomposition of turbulent channel flow', *International Journal of Numerical Methods Fluids*, Vol. 21, pp.585–598.

Bernero, S. and Fiedler, H.E. (2000) 'Application of particle image velocimetry and proper orthogonal decomposition to the study of a jet in a counterflow', *Experiments in Fluids*, Vol. 29, pp.S274–S281.

Cai, W.H., Li, F.C., Zhang, H.N., Li, X.B., Yu, B., Wei, J.J., Kawaguchi, Y. and Hishida, K. (2009) 'Study on the characteristics of turbulent drag-reducing channel flow by particle image velocimetry combining with proper orthogonal decomposition analysis', *Physics of Fluids*, Vol. 21, pp.115103-1~115103-12.

Dean, R.B. (1978) 'Reynolds number dependence of skin friction and other bulk flow variables in two-dimensional rectangular duct flow', *Transactions of ASME, Journal of Fluids Engineering*, Vol. 100, pp.215–223.

Deane, A.E., Kevrekidis, I.G., Karniadakis, G.E. and Orszag, S. (1991) 'Low dimensional models for complex geometry flows: application to grooved channels and circular cylinder', *Physics of Fluids A*, Vol. 3, pp.2337–2354.

Druault, P. and Chaillou, C. (2007) 'Use of proper orthogonal decomposition for reconstructing the 3D in-cylinder mean-flow field from PIV data', *Compute Rendus Mecanique*, Vol. 335, pp.42–47.

Gatski, T.B. and Glauser, M.N. (1992) *Proper Orthogonal Decomposition based Turbulence Modelling. Instability, Transition and Turbulence*, Springer-Verlag, New York.

Gurka, R., Liberzon, A. and Hetsroni, G. (2006) 'POD of vorticity fields – a method for spatial characterization of coherent structures', *International Journal of Heat and Fluid Flow*, Vol. 27, pp.416–423.

Kagawa, Y., Yu, B., Kawaguchi, Y., Kawamura, K. and Shiraishi, Y. (2008) 'Turbulent heat transfer of viscoelastic fluid flow accompanied by drag reduction with DNS analysis', *Progress in Computational Fluid Dynamics*, Vol. 8, pp.477–485.

Kays, W.M. and Crawford, M.E. (1980) *Convective Heat and Mass Transfer*, 2nd ed., McGraw-Hill, New York.

Laurent, G., Marc, M. and Nathalie, G. (2001) 'Combining PIV, POD and vortex identification algorithms for the study of unsteady turbulent', *Measurement Science and Technology*, Vol. 12, pp.1422–1429.

Lumley, J.L. (1967) 'The structure of inhomogeneous turbulent flows', in Yaglom, A.M. and Tatarski, V.I. (Eds.): *Atmospheric Turbulence and Radio Wave Propagation*, Nauka, Moscow, pp.166–178.

Moin, P. and Moser, R.D. (1989) 'Characteristic-eddy decomposition of turbulence in channel', *Journal of Fluid Mechanics*, Vol. 200, pp.471–509.

Payne, F.R. and Lumley, J.L. (1967) 'Large-eddy structure of the turbulent wake behind a circular cylinder', *Physics of Fluids*, Vol. 10, pp.194–196.

Rajaee, M., Karlsson, S.K.F. and Sirovich L. (1994) 'Low dimensional description of free shear flow coherent structure and their dynamical behavior', *Journal of Fluid Mechanics*, Vol. 258, pp.1–29.

Rempfer, D. and Fasel, H.F. (1994a) 'Dynamics of three dimensional coherent structures in a flat-plate boundary layer', *Journal of Fluid Mechanics*, Vol. 275, pp.257–283.

Rempfer, D. and Fasel, H.F. (1994b) 'Evolution of three dimensional coherent structures in a flat-plate boundary layer', *Journal of Fluid Mechanics*, Vol. 260, pp.351–375.

Shi, L.L., Liu, Y.Z. and Wan, J.J. (2010) 'Influence of wall proximity on characteristics of wake behind a square cylinder: PIV measurements and POD analysis', *Experimental Thermal and Fluid Science*, Vol. 34, pp.28–36.

Sirovich, L. (1987) 'Turbulent and dynamics of coherent structure: I-III', *Quarterly of Applied Mathematics*, Vol. 45, pp.561–590.

Wang, Y., Yu, B., Wei, J.J., Li, F.C. and Kawaguchi, Y. (2009) 'Direct numerical simulation on drag-reducing flow by polymer additives using a spring-dumbbell model', *Progress in Computational Fluid Dynamics*, Vol. 9, pp.217–224.

Yang, X., Peng, D., Li, Z.Y. and Tao, W.Q. (2010) 'Extraction and analysis of turbulent large scales based on POD method', *Journal of Engineering Thermophysics*, Vol. 31, pp.1019–1022 (in Chinese).

Yu, B. and Kawaguchi, Y. (2005) 'DNS of fully developed turbulent heat transfer of a viscoelastic drag-reducing flow', *International Journal of Heat and Mass Transfer*, Vol. 48, pp.4569–4578.

Yu, B. and Kawaguchi, Y. (2004) 'Direct numerical simulation of viscoelastic drag-reducing flow: a faithful finite difference method', *Journal of Non-Newtonian Fluid Mechanics*, Vol. 116, pp.431–466.

Yu, B., Wu, X., Wei, J.J., Li, F.C. and Kawaguchi, Y. (2011) 'DNS study by a bilayer model on the mechanism of heat transfer reduction in drag-reduced flow induced by surfactant', *International Communications in Heat and Mass Transfer*, Vol. 38, pp.160–167.

## Nomenclature

| | |
|---|---|
| $A$ | Eigenvector |
| $C$ | The inner product in the Hilbert space |
| $C_f$ | Friction factor $=2\tau_w/\rho u_m^2$ |
| $C_f^D$ | Friction factor by Dean's equation |
| $c$ | Conformation tensor |
| $c_p$ | Specific heat at constant pressure (J/(kg·K)) |
| $DR$% | Drag reduction rate |
| $E$ | Total energy of fluctuating field |
| $F$ | Common variable for instantaneous velocity and temperature |
| $f'$ | Reconstructed fluctuating field |
| $F'$ | Common variable for fluctuating velocity and temperature |
| $HTR$% | Heat transfer reduction rate |
| $h$ | Half height of the channel (m) |
| $h^*$ | Heat transfer coefficient (W/(m$^2$·K)) |
| $k$ | Thermal conductivity (W/(m·K)) |
| $N$ | Number of snapshots |
| $Nu$ | Nusselt number $=2h^*h/k$ |
| $Nu^K$ | Nusselt number by Kays and Crawford's equation |
| $Pr$ | Molecular Prandtl number |
| $p$ | Pressure (Pa) |
| $q_w$ | Wall heat flux (W/m$^2$) |
| $Re_m$ | Reynolds number $=2\rho u_m h/\eta_s$ |
| $Re_\tau$ | Reynolds number $=\rho u_\tau h/\eta_s$ |
| $t$ | Time (s) |
| $t^*$ | Dimensionless time $=t/(u_\tau/h)$ |
| $T$ | Temperature (°C, K) |
| $T_m$ | Bulk mean temperature (°C, K) |
| $T_\tau$ | Friction temperature $=q_w/(\rho c_p u_\tau)$ (°C, K) |
| $u$ | Velocity (m/s) |
| $u_m$ | Mean velocity (m/s) |
| $u_\tau$ | Friction velocity $=\sqrt{\tau_w/\rho}$ (m/s) |
| $We_\tau$ | Weissenberg number $=\rho\lambda u_\tau^2/\eta_s$ |
| $x_1, x$ | Streamwise direction (m) |
| $x_2, y$ | Wall-normal direction (m) |
| $x_3, z$ | Spanwise direction (m) |
| $\vec{X}$ | Common variable for dimensionless coordinates |
| *Greek symbols* | |
| $\alpha$ | Mobility factor |
| $\alpha_k$ | Temporal coefficient of the $k$th POD mode |
| $\beta$ | Ratio $=\eta_a/\eta_s$ |
| $\delta$ | Kronecker symbol |
| $\phi_n$ | $n$th eigenmode |
| $\eta_a$ | Dynamic shear viscosity of surfactant contribution (Pa·s) |
| $\eta_s$ | Dynamic shear viscosity of solvent contribution (Pa·s) |
| $\eta_0$ | Shear viscosity of the surfactant solution at zero-shear rate $=\eta_a+\eta_s$ (Pa·s) |
| $\lambda$ | Relaxation time (s) |
| $\lambda_n$ | Eigenvalue of the $n$th POD mode |
| $\Theta$ | Par mean local temperature (°C, K) |
| $\Theta_m$ | Mixed mean temperature (°C, K) |
| $\theta$ | Local temperature difference $=\overline{T_w}-T$ (°C, K) |
| $\rho$ | Density (kg/m$^3$) |
| $\tau_w$ | Statistically averaged wall shear stress (Pa) |
| $\xi_n$ | Energy relative contribution to the total energy in the $n$th eigenmode |
| $\zeta_n$ | Cumulative energy relative contribution to the total energy |
| *Superscripts and subscripts* | |
| $(\,)^+$ | Normalised by $u_\tau$, $\rho$, $\eta_s$ and $T_\tau$ |
| $(\,)^*$ | Dimensionless coordinate ($x$, $y$ and $z$) |
| $(\,)_{\rm rms}$ | Fluctuation intensities |
| — | Ensemble average over the spanwise direction and time |